Proceedings of the ASME 2020 Conference on Smart Materials, Adaptive Structures and Intelligent Systems
SMASIS2020
September 15, 2020, Virtual, Online

SMASIS2020-2292

ENHANCING ADAPTABLE TOPOLOGICAL WAVE BANDWIDTH IN PIEZOELECTRIC METAMATERIALS VIA CIRCUITRY AND LATTICE SYMMETRY CONTROL

Patrick Dorin[1], K.W. Wang
Department of Mechanical Engineering
University of Michigan
Ann Arbor, Michigan

ABSTRACT

Recently, an electromechanical metamaterial with integrated resonant circuit elements was developed that enables on-demand tailoring of the operating frequency and interface routes for topological wave transmission. However, limitations to the operating frequency region still exist, and a full exploration of the adaptive characteristics of the topological electromechanical metamaterial has yet to be undertaken. To advance the state of the art, this study investigates the ability to enhance the range of operating frequencies for topological wave transmission in a piezoelectric metamaterial by the reconfiguration of lattice symmetries and connection of negative capacitance circuitry. In addition, the capability to modify the interface mode localization is analyzed. The plane wave expansion method is utilized to define a working frequency region for protected topological wave transmission by evaluating a local topological charge. Numerical simulations verify the existence of topologically protected interface modes and illuminate how the localization and shape of these modes can be altered via external circuit parameters. Results show that the reconfiguration of the lattice structure and connection to negative capacitance circuity enhances the operating frequency bandwidth and interface mode localization control, greatly expanding the adaptive metamaterial capabilities.

Keywords: topological, metamaterial, piezoelectric, negative capacitance, quantum valley Hall, adaptive

1 INTRODUCTION

Topological metamaterials are being extensively investigated as a means to achieve a variety of protected elastic wave control phenomena [1,2]. Unlike wave propagation in conventional waveguides, topologically protected wave transmission is immune to lattice imperfections and disorder such as sharp corners that are often present in practical engineering applications. The unique characteristics of topologically protected wave propagation in elastic waveguides could be leveraged for performance enhancement in applications such as vibration isolation, wave control, cloaking, energy harvesting, sensing, and wave filtering [3]. Initial investigations extended the theories of topological transport from quantum mechanics to elastic metamaterials and successfully demonstrated topologically protected wave transmission in elastic waveguides [4–10]. The initially designed elastic topological metamaterials were comprised of inflexible/fixed geometric structures (e.g., perforated plates) or contained complex moving parts (e.g., gyroscopes), which limited the practical implementation of these concepts. To build upon the initial demonstrations, further studies have incorporated adaptivity into elastic topological metamaterials, broadening their functionalities and making them more adaptive to ever-changing external operating conditions. Many of these adaptive topological realizations have used an external bias, such as a mechanical force [11–13], thermal gradient [14], or magnetic field [15], to induce changes to topological properties of a lattice structure. In addition, piezoelectric topological metamaterials have been investigated due to their ease of integration into conventional load-bearing structures and real-time tunability through external circuitry [16–18]. With each of the described adaptive methods, it was demonstrated that local changes to lattice topological properties enabled control over the protected wave propagation route within a metamaterial. Yet, the majority of adaptive topological wave propagation studies to date have not analyzed far beyond switching of propagation routes. To enhance the adaptive capabilities of topological metamaterials, a

[1] Contact author: pdorin@umich.edu

piezoelectric metamaterial that enables reconfiguration of both the operating frequency and interface path for topologically protected transmission was recently introduced [19]. However, an unexplored opportunity remains to identify and expand the effective operating frequency region for protected transmission and conduct a comprehensive exploration of the rich adaptive functionalities of the topological piezoelectric metamaterial. Thus, to advance the state of the art, this research proposes the connection of negative capacitance circuitry and reconfiguration of lattice symmetries to enhance the adaptive capabilities of a piezoelectric metamaterial. An analysis is conducted to demonstrate how negative capacitance circuitry and adjustable lattice symmetries can be leveraged to enhance topological wave bandwidth and enable adjustments to the shape of the interface mode. The piezoelectric metamaterial for this study is comprised of a thin composite plate with piezoelectric and aluminum mechanical constituents that is connected to external circuitry via conductive electrodes placed in a honeycomb lattice arrangement. The honeycomb lattice arrangement of electrodes contains the symmetries required to generate the elastic analog of the quantum valley Hall effect (QVHE) and achieve topologically protected interface states. Since the topological characteristics of the system arise from the lattice arrangement of electrodes, the tailoring of topological wave propagation is facilitated solely by the connected circuitry. On the other hand, the mechanical geometry is a simple load-bearing structure (thin plate) that can remain unaltered. In the proposed approach, the external circuitry contains an inductor to create a resonant circuit and a capacitor for the application of a negative capacitance. The inductor in the resonant circuit is used to tune the frequency of the topological interface state over an operating range where topological protection is achievable. The negative capacitance circuitry is used to synthetically enhance the electromechanical coupling (as demonstrated in [20,21]), which in turn increases the topological wave bandwidth and enables improved interface mode localization. Lattice symmetries are reconfigured using the external circuitry to further enhance the topological operating bandwidth and facilitate additional interface modes.

The following manuscript is organized as follows. Sec. 2 includes a description of the metamaterial and mathematical model. In Sec. 3, the working principle and achievable operating region for topologically protected wave propagation is identified. Sec. 4 includes an analysis on how to enhance the achievable operating region and increase interface mode localization using negative capacitance circuitry. In Sec. 5, further adaptivity enhancements through lattice symmetry reconfiguration are investigated. Finally, overall discussion and conclusions are presented in Sec. 6.

2 SYSTEM DESCRIPTION AND MATHEMATICAL MODEL

2.1 System Description

The schematic for the piezoelectric metamaterial is shown in Fig. 1. The metamaterial is made up of a thin plate with an aluminum substrate (gray) of thickness h_s that is sandwiched by

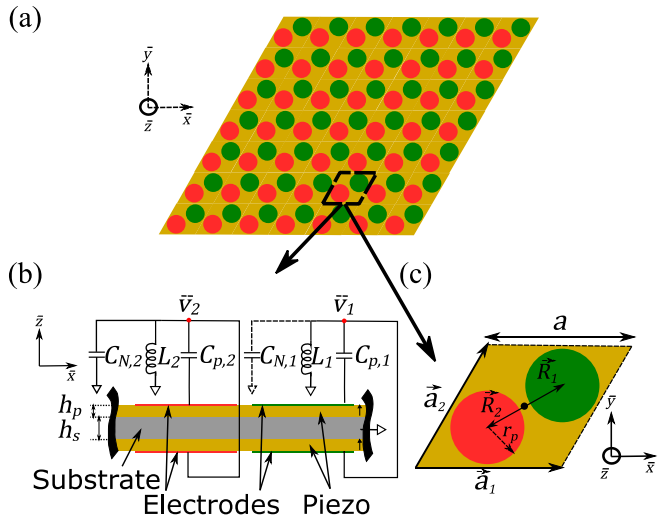

FIGURE 1: (a) Schematic of the metamaterial honeycomb lattice arrangement. Unit cell is enclosed in dashed box, green indicates electrode geometry connected to circuit 1, red indicates electrode geometry connected to circuit 2. (b) Cross-section and (c) top view of the unit cell.

piezoelectric plates (yellow) of thickness h_p. The aluminum substrate has elastic modulus E_s, density ρ_s, and Poisson's ratio ν_s. The piezoelectric elements have density ρ_p, elastic constant $\bar{c}_{11}^E$, and effective piezoelectric constant $\bar{e}_{31}$. The piezoelectric constituents are connected to external circuitry by conductive electrodes that are placed in a honeycomb lattice arrangement, as shown in Fig. 1a. The basis vectors that define the triangular unit cell of the metamaterial (dashed box of Fig. 1a) are $\vec{a}_1 = a\hat{\imath}$ and $\vec{a}_2 = a\left(\cos\frac{\pi}{3}\hat{\imath} + \sin\frac{\pi}{3}\hat{\jmath}\right)$, where a is the characteristic length (Fig. 1c). The unit cell contains two electrode pairs that create two capacitors with capacitances of $C_{p,1}$ and $C_{p,2}$ (Fig. 1b). Each capacitor is connected to an external inductor L_j to form a resonant circuit with resonant frequency $\omega_{t,j} = \sqrt{\frac{1}{L_j C_{p,j}}}$ for the jth circuit. In addition, an external negative capacitor is connected in parallel, with negative capacitance $C_{N,j}$. It is assumed that all circuit elements are ideal, and thus all ohmic losses are assumed negligible.

2.2 Mathematical Model

The system governing equations that govern flexural displacement $\bar{w}(\bar{x},\bar{y},t)$ of the plate and voltage response $\bar{v}_j(t)$ of the jth electrode pair are derived using the extended Hamilton's principle [22] in conjunction with the linear theory of piezoelectricity [23] and the classical theory of thin plates [24]. A harmonic response at frequency ω is assumed, non-dimensional variables are introduced, and the non-dimensional governing equations are given by Eq. 1:

$$\left(\nabla^4 - \frac{\omega^2 m a^4}{D_T}\right) w(r) - \sum_{j=1}^{N_e} \frac{\theta^2 a^2}{(C_{p,j}-C_{N,j})D_T} \nabla^2 v_j \chi_j(r) = 0 \quad (1a)$$

$$\left(1 - L_j(C_{p,j} - C_{N,j})\omega^2\right) v_j - \omega^2 L_j (C_{p,j} - C_{N,j}) \iint_{D_j} \nabla^2 w(r)\, d^2 r = 0, \quad j = 1 \ldots . N_e \text{ electrode pairs} \quad (1b)$$

where the non-dimensional flexural displacement, voltage, time, and length scales are defined as $w = \frac{\bar{w}}{a}, v_j = \frac{1}{a}\frac{C_{p,j}-C_{N,j}}{\theta}\bar{v}_j, \tau = \sqrt{\frac{1}{L_j(C_{p,j}-C_{N,j})}}t$, $x = \frac{\bar{x}}{a}$, $y = \frac{\bar{y}}{a}$, and $z = \frac{\bar{z}}{a}$, respectively, $r = (x, y)$, $m = \rho_s h_s + 2\rho_p h_p$ is the mass per unit area, $D_T = D_s + D_p = \frac{E_s h_s^3}{12(1-\nu_s^2)} + \bar{c}_{11}^E \left(\frac{2h_p^3}{3} + h_p^2 h_s + \frac{h_p h_s^2}{2}\right)$ is the effective flexural rigidity of the plate at short circuit, $\theta = \bar{e}_{31}(h_p + h_s)$ is an electromechanical coupling coefficient, L_j, $C_{p,j}$, and $C_{N,j}$ are the inductance, piezoelectric capacitance, and negative capacitance for the jth electrode pair, ∇^2 and ∇^4 are the dimensionless Laplacian operator and dimensionless biharmonic operator, respectively, N_e is the total number of electrode pairs, and the step-function $\chi_j(r) = \begin{cases} 1, & r \in D_j \\ 0, & otherwise \end{cases}$ is defined in terms of the dimensionless domain D_j of the jth electrode pair.

Next, the plane wave expansion (PWE) method [19,25] is used to determine the dispersion relation for the metamaterial from the periodic unit cell. As shown in Fig. 1b, the unit cell contains two circuits (corresponding to the two electrode pairs) $N_e = 2$. The circuits are defined as having inductance parameters $L_1 = L(1+\beta)$ and $L_2 = L(1-\beta)$, where β is the circuit inductance perturbation parameter. Per the PWE method, the non-dimensional dispersion relation is defined as a superposition of plane waves, per Eq. 2:

$$w(r) = \sum_G W(G) e^{-ia(k+G)\cdot r}, G = m\vec{b}_1 + n\vec{b}_2, \quad m, n \in [-M, M], \quad k = (k_x, k_y) \quad (2)$$

where G is the reciprocal lattice vector, m and n are the plane wave indices, $\vec{b}_1 = \frac{\pi}{a}\left(2\hat{\imath}, -\frac{2}{\sqrt{3}}\hat{\jmath}\right)$ and $\vec{b}_2 = \frac{\pi}{a}\left(0\hat{\imath}, \frac{4}{\sqrt{3}}\hat{\jmath}\right)$ are the reciprocal lattice basis vectors (see Fig. 2a inset for reciprocal lattice diagram), k is the Bloch wavevector, and $N^2 = (2M+1)^2$ is the number of plane waves specified for the calculation. Substituting Eq. 2 into Eq. 1 leads to Eq. 3:

$$(a^4|k+G|^4 - \Omega^2) W(G) + \sum_{j=1}^{N_e} \frac{\vartheta}{1-\xi_j} \frac{a^2}{A_c} \frac{a^2}{A_{e,j}} a^2 |k+G|^2 \iint_{D_j} v_j e^{ia(k+G)\cdot r} d^2 r = 0 \quad (3a)$$

$$\left(\frac{\Omega_{t,j}^2}{(1-(-1)^j\beta)(1-\xi_j)} - \Omega^2\right) v_j + \Omega^2 a^2 \sum_G W(G)|k+G|^2 \iint_{D_j} e^{-ia(k+G)\cdot r} d^2 r = 0, \quad j = 1 \ldots . N_e \text{ electrode pairs} \quad (3b)$$

where $\Omega = \omega a^2 \sqrt{\frac{m}{D_T}}$ is non-dimensional frequency, $\Omega_{t,j} = \sqrt{\frac{1}{LC_{p,j}}} a^2 \sqrt{\frac{m}{D_T}}$ is the non-dimensional circuit tuning frequency, $\xi_j = \frac{C_{N,j}}{C_{p,j}}$ is the negative capacitance ratio for the jth circuit, $\vartheta = \frac{\theta^2}{\hat{c}_p D_T}$ is the non-dimensional electromechanical coupling coefficient, A_c is the area of the unit cell, and $A_{e,j}$ is the area within the unit cell containing the jth electrode pair. While the derived model is general, in this study: $C_{N,j} = C_N$, $C_{p,j} = C_p$, and $A_{e,j} = A_e$, such that $\Omega_{t,j} = \Omega_t$ and $\xi_j = \xi$.

3 DISPERSION ANALYSIS

In this section, a dispersion analysis is conducted to evaluate the band structure of the metamaterial and demonstrate the working principle for the achievement of tunable topologically protected edge states. In a case study (Sec. 3.1), critical metrics are

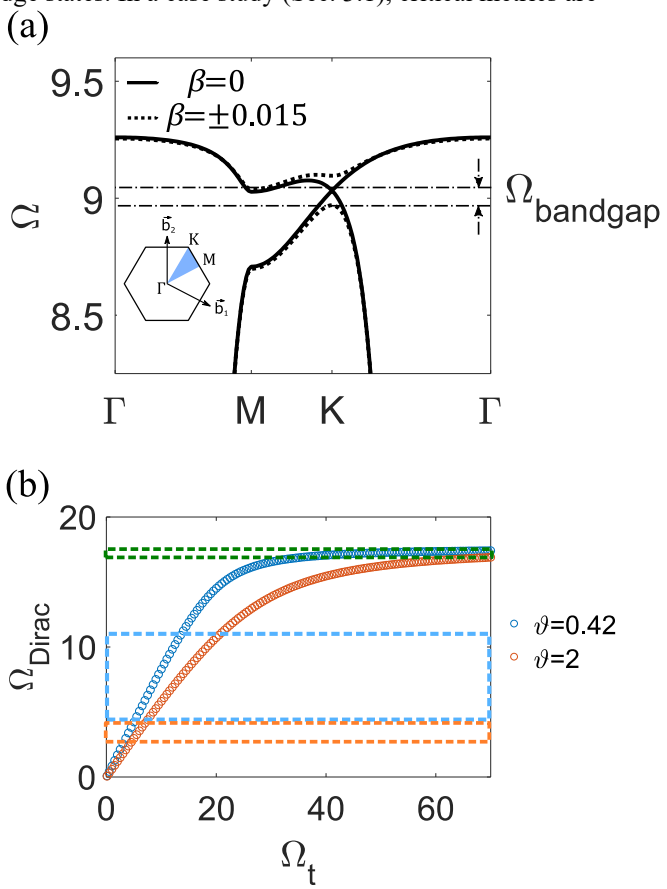

FIGURE 2: (a) Band structure of unit cell showing Dirac point (solid line, $\beta = 0$) and broken SIS (dashed line, $\beta = \pm 0.015$). Full bandgap $\Omega_{bandgap}$ for broken SIS is enclosed by dash-dot lines. Inset contains diagram of reciprocal lattice and IBZ. (b) Non-dimensional Dirac frequency Ω_{Dirac} as a function of non-dimensional circuit tuning frequency Ω_t for different electromechanical couplings $\vartheta = 0.42$ (blue) and $\vartheta = 2$ (orange). Blue box encloses achievable operating region for topological interface state with $\vartheta = 0.42$ (Sec. 3.2), orange box indicates achievable operating region enhancement from negative capacitance circuitry $\vartheta_{NC} = 2$ (Sec. 4), and green box indicates operating region enhancement from lattice reconfiguration (Sec. 5).

identified to predict the performance of a topological waveguide from unit cell design. An achievable operating region is then identified through a parametric analysis (Sec 3.2) of circuit tuning parameters to assess the adaptivity of the metamaterial.

3.1 Dispersion Analysis – Case Study

Equation 3 can be recast as the classical eigenvalue problem $([\mathbf{K}]-\Omega^2[\mathbf{M}])[\{W_{m,n}\} \quad v_1 \quad v_2]^T = 0$. The dispersion relation is evaluated by specifying the Bloch wavevector k to follow the boundary of the irreducible Brillouin zone (see blue triangle in inset of Fig. 2a) while solving for non-dimensional frequency Ω. For this case study, a = 0.04 m, $A_e = \pi\left(0.92\frac{\sqrt{3}}{6}a\right)^2$ m^2, h_p and h_s are both 1 mm, and aluminum (ρ_s = 2700 kg/m^3, E_s = 70 GPa) and PZT-5H (ρ_p = 7500 kg/m^3 and $\bar{c}_{11}^E$= 66.2 GPa , $\bar{e}_{31}$ = -23.4 C/m^2) are selected as the materials, resulting in ϑ = 0.42. The circuit parameters are selected such that Ω_t = 11 and there is no negative capacitance (ξ = 0). Evaluation of the band structure indicates that for equal circuit inductance parameters (β = 0) there exists a degeneracy between the first and second bands at the K-point that is referred to as a Dirac Point (solid line, Fig. 2a). This Dirac point is protected by C_3 lattice symmetry, space inversion symmetry (SIS), and time-reversal symmetry (TRS) [2]. The frequency of the Dirac point (Ω_{Dirac}) is less than the circuit tuning frequency Ω_t. Due to the resonant nature of the circuits, the Dirac frequency can be tailored through a range covering Ω_{Dirac}= 0 and Ω_{Dirac}= 17.6 by changing the external circuit frequency parameter Ω_t (Fig. 2b).

The elastic analog of the QVHE [2,26] is utilized to achieve a topologically protected waveguide. SIS is broken by specifying different inductance parameters for each circuit in the unit cell ($\beta \neq 0$), and a full bandgap is opened from the Dirac point at the Dirac frequency Ω_{Dirac} (Fig. 2a, dashed line is band structure with $\beta = \pm 0.015$, arrows indicate bandgap $\Omega_{bandgap}$). To provide an equivalent metric that does not bias towards certain frequency ranges, the size of the bandgap is normalized ($\Omega_{bandgap-relative}$) as shown in Eq. 4:

$$\Omega_{bandgap-relative} = \frac{\Omega_{2-min}-\Omega_{1-max}}{\frac{\Omega_{2-min}+\Omega_{1-max}}{2}} = \frac{2\Omega_{bandgap}}{\Omega_{2-min}+\Omega_{1-max}} \quad (4)$$

where Ω_{p-min} and Ω_{p-max} represent the minima and maxima of the pth band. Lattices with $\beta > 0$ (Type A) and $\beta < 0$ (Type B) contain identical band structures (Fig. 2a, dashed line for $\beta = \pm 0.015$). However, a band inversion exists between Type A and Type B lattices, meaning eigenvectors $u_p(k)$ associated with the pth band are interchanged. This band inversion grants the lattices distinct topological characteristics. The topological characteristics of the lattice are quantified by the valley Chern number C_{v-p}, a topological charge that is defined as the integral of the Berry Curvature $B_p(k) = -\nabla_k \times \langle u_p(k)|i\nabla_k[\mathbf{M}]|u_p(k)\rangle$ near the K-point for the pth band as shown in Eq. 5 [4,27,28].

$$C_{v-p} = \frac{1}{2\pi}\iint_v B_p(k)d^2k \quad (5)$$

The theoretical valley Chern values are C_{v-1}^A= -0.5 and C_{v-2}^A = 0.5 for a Type A lattice and C_{v-1}^B= 0.5 and C_{v-2}^B = -0.5 for a Type B lattice [4,28]. To construct a topological waveguide, Type A and Type B lattices are joined at an interface to create a topological transition. This topological transition enables topologically protected edge states [28,29] with localized flexural displacement at the interface (interface state), as shown in [19].

The interface state can be isolated from bulk modes and activated at a frequency within the bandgap that is opened from the Dirac point. Thus, the largest potential operating bandwidth of the interface state for a given set of specified metamaterial parameters is defined by the size of the bandgap (Eq. 4). The level of topological protection for the interface state, or its robustness to lattice imperfections and disorder, that results from the QVHE is dependent on the localization of the Berry curvature [30,31]. This localization is measured by the magnitude of the valley Chern number (Eq. 5), and thus a larger magnitude of valley Chern number $|C_{v-p}|$ indicates increased robustness. For this study, the performance of the interface state will be evaluated by its potential operating bandwidth and level of topological protection. Therefore, to predict the performance of the topological waveguide for a defined set of system parameters, $\Omega_{bandgap-relative}$ (Eq. 4) and C_{v-p} (Eq. 5) are calculated for the unit cell. For the circuit parameters specified in this case study ($|\beta|$ = 0.015, Ω_t = 11, ξ = 0) the topological charges are calculated as: C_{v-1}^A= -0.3 and C_{v-2}^A = 0.3 for a Type A lattice (β = 0.015) and C_{v-1}^B= 0.3 and C_{v-2}^B = -0.3 for a Type B lattice (β = -0.015). The magnitude of the calculated topological charge $|C_{v-calculated}|$= 0.3 is less than the theoretical maximum value $|C_{v-theoretical}|$= 0.5. The calculated magnitude of the topological charge is less than the idealized value because of the relatively large perturbation applied to the lattice [4,32], but its nontrivial value indicates nontrivial topological characteristics and the emergence of a topologically protected interface state. In fact, in previous studies, it has been shown that $|C_{v-p}| \geq 0.3$ has been sufficient to achieve robust wave propagation in a topological waveguide [4,32]. The maximum potential operating bandwidth for an interface state with the selected circuit parameters is indicated by the normalized bandgap $\Omega_{bandgap-relative}$ = 0.007.

3.2 Dispersion Analysis – Parametric Study

In contrast to most previously studied adaptive elastic topological metamaterials, the piezoelectric metamaterial analyzed in this study enables real-time, continuously reconfigurable frequency, location, and shape of interface states [19]. Thus, due to the comprehensive tunability of the piezoelectric metamaterial, a case study only demonstrates the working principle and performance for a specific set of parameters. A parametric study is conducted to define an achievable operating region and fully explore the adaptive capabilities of the metamaterial. The computational efficiency of the mathematical model developed using the PWE method (Eq. 3) facilitates the parametric study. For the analysis, the previously discussed performance metrics $\Omega_{bandgap-relative}$ (Eq. 4) and C_{v-p} (Eq. 5) are evaluated for a wide range of tunable circuit parameters (β and Ω_t), with the mechanical geometry

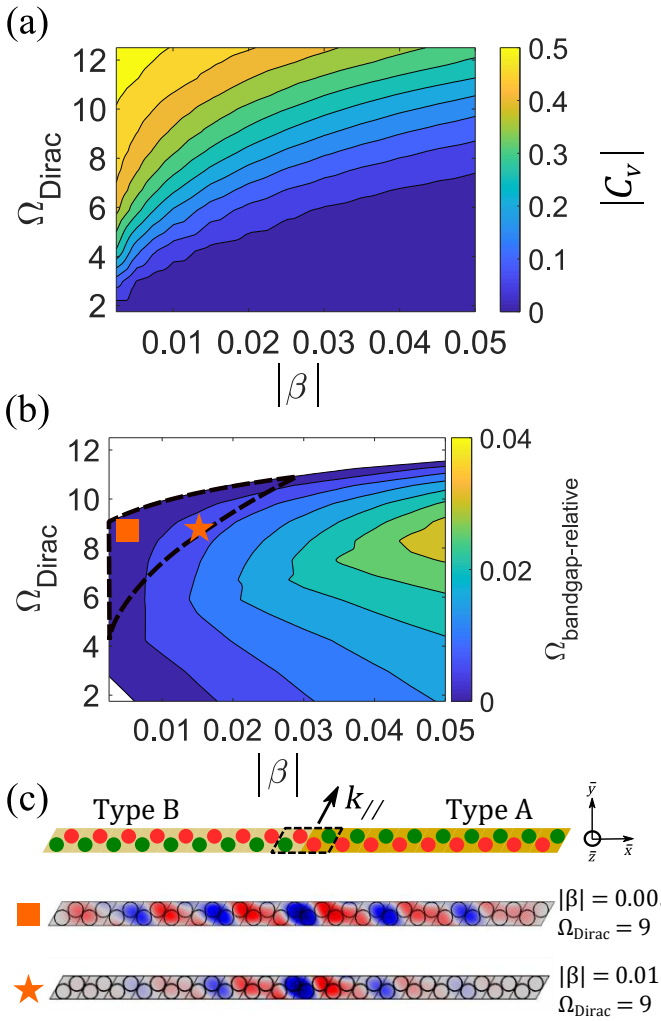

FIGURE 3: (a) Magnitude of valley Chern number $|C_v|$ as a function of $|\beta|$ and Ω_{Dirac} for unit cell of metamaterial with $\xi = 0$ and $\vartheta = 0.42$. Increasing brightness indicates increasing $|C_v|$. (b) Relative bandgap $\Omega_{bandgap-relative}$ as a function of $|\beta|$ and Ω_{Dirac} for unit cell of metamaterial with $\xi = 0$ and $\vartheta = 0.42$. Increasing brightness indicates larger $\Omega_{bandgap-relative}$. Achievable operating region for topological interface state is enclosed by dashed black line. (c) Finite strip that contains an interface (enclosed by dashed black box) between Type A and Type B unit cells. Interface mode shapes that are generated from dispersion analysis of finite strip defined with unit cell parameters indicated by ■ and ★ markings in (b).

remaining constant. Figure 3a shows the magnitude of the valley Chern number for band 1 of a Type A lattice $|C^A_{v-1}|$ as a function of circuit inductance perturbation $|\beta|$ and Dirac frequency Ω_{Dirac} (note: Ω_{Dirac} is controlled by specifying Ω_t per Fig. 2b). The $|C_v|$ result shown in Fig. 3a is general and can be applied to band 1 or band 2 of Type A or Type B unit cells because calculations indicate that $C^A_{v-1} = C^B_{v-2} \approx -C^A_{v-2} = -C^B_{v-1} \therefore |C^A_{v-p}| \approx |C^B_{v-p}|$ for p = 1,2. Figure 3a demonstrates that, for fixed Ω_{Dirac}, the localization of the Berry curvature (indicated by $|C_v|$) decreases as the magnitude of the perturbation $|\beta|$ to the circuit inductance

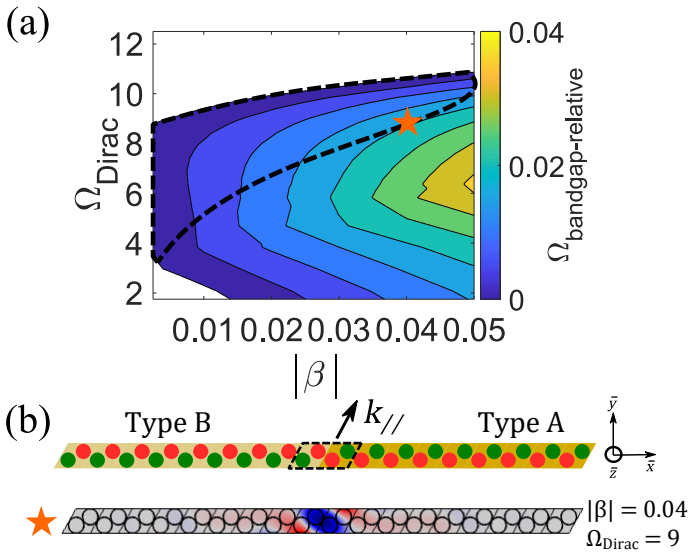

FIGURE 4: (a) Relative bandgap $\Omega_{bandgap-relative}$ as a function of $|\beta|$ and Ω_{Dirac} for unit cell of metamaterial with negative capacitance circuitry (ξ= 0.79 and ϑ_{NC} = 2). Increasing brightness indicates larger $\Omega_{bandgap-relative}$. Achievable operating region for topological interface state enclosed by black dashed lines. (b) Finite strip that contains an interface (enclosed in black dashed lines) between Type A and Type B unit cells. Interface mode shape that is generated from dispersion analysis of finite strip defined with unit cell parameters indicated by ★ marking in (a).

parameter is made larger. Figure 3b shows the relative bandgap $\Omega_{bandgap-relative}$ as a function of $|\beta|$ and Ω_{Dirac}. In contrast to $|C_v|$, $\Omega_{bandgap-relative}$ increases with increasing $|\beta|$ for a given Ω_{Dirac}. This tradeoff between topological robustness and potential operating bandwidth under fixed system parameters is commonplace in elastic metamaterials exhibiting the QVHE [30,32]. However, the frequency tunability of the proposed piezoelectric metamaterial grants an alternative avenue to enhance the frequency range for the realization of topological interface states. Since the bandgap where the interface state is contained is opened from the Dirac point, the frequency of the interface state is near Ω_{Dirac}, and thus can be controlled using circuit parameters. Per Fig. 3a, nontrivial values of $|C_v|$, which indicate the emergence of topologically protected interface states, are exhibited over a large range of Dirac frequencies Ω_{Dirac}. However, to realize a topological interface state that is readily isolated from bulk modes, there must be a full bandgap opened from the Dirac point. Thus, to realize an isolated topological interface state with a sufficient level of robustness, $|C_v|$> 0.3 (per discussion in Sec. 3.1) and $\Omega_{bandgap-relative} > 0$. These constraints define the achievable operating region, which is shown as the region enclosed in black dashed lines in Fig. 3b. This operating region spans Ω_{Dirac} = 4.2 to Ω_{Dirac} = 11. Circuit parameters can be tuned through this entire frequency range to change the frequency of the interface state. The frequency tunability of the interface state gives the metamaterial the capability to adapt to changing operating requirements or

external conditions. In addition, the identification of the achievable operating region reveals that while the Dirac frequency can be varied over the region containing $\Omega_{Dirac} = 0$ and $\Omega_{Dirac} = 17.6$ using Ω_t (Fig. 2b), the actual frequency region where sufficiently protected interface states can emerge is only a subset of this (see the blue box in Fig. 2b).

Apart from frequency, the continuous tunability of the resonant circuits can also be used to vary the localization and shape of the interface mode within the achievable operating region. Within this achievable region, the perturbation to the circuit inductance can be tuned between $|\beta| = 0$ and $|\beta| = 0.03$ (Fig. 3b). To study the effect of varying $|\beta|$ on the interface state, the interface mode shapes are obtained by using COMSOL finite element software. COMSOL is used to evaluate the band structure of a finite width strip containing an interface between Type A and Type B lattices (Fig. 3c). The edges of the finite strip are fixed and a periodic condition is applied in the $k_{//}$ direction. Figure 3c contains examples of two interface mode shapes from the band structure that are taken from the band containing the interface state. For a fixed Dirac frequency $\Omega_{Dirac} = 9$, $|\beta|$ is increased from $|\beta| = 0.005$ (■ in Fig. 3c) to $|\beta| = 0.015$ (★ in Fig. 3c). These mode shapes show how displacement localization at the interface can be enhanced by selecting a larger $|\beta|$ for a given Ω_{Dirac}, due to an increase in the magnitude of band inversion between Type A and Type B unit cells. Therefore, circuit parameters can be used to tailor the displacement localization of the interface mode shape within the achievable operating region.

The definition and exploration of the achievable operating region in this section is an important consideration that has yet to be addressed in other adaptive topological elastic wave investigations. Constrained to this operating region, circuit parameters for the piezoelectric metamaterial can be utilized to tailor the interface state frequency and displacement localization while achieving a desired level of topological protection and potential operating bandwidth.

4 NEGATIVE CAPACITANCE CIRCUITRY

Negative capacitance circuitry has previously been used to broaden bandgaps in piezoelectric metamaterials by enhancing the electromechanical coupling [20,21]. In this study, negative capacitance circuitry is used to enhance the electromechanical coupling ϑ, and the effect on the adaptive topological interface state is investigated.

To introduce negative capacitance to each circuit, an ideal negative capacitor C_N is connected in parallel (as shown in Fig. 1b), with the negative capacitance ratio defined as $\xi = \frac{C_N}{C_p} \neq 0$ in Eq. 3. As can be observed in Eq. 3, the result of adding negative capacitance is an enhanced electromechanical coupling coefficient of $\vartheta_{NC} = \frac{\vartheta}{1-\xi}$ and an adjusted circuit tuning frequency of $\Omega_{t-NC} = \frac{\Omega_t}{\sqrt{1-\xi}}$. All other Eq. 3 parameters are unchanged, and thus the working principle (Sec. 3) that defines performance and adaptivity for the piezoelectric metamaterial remains qualitatively the same. With the addition of negative capacitance circuitry, the electromechanical coupling ϑ_{NC} can theoretically approach an infinitely large value. However, since negative capacitance is realized with an active element, practical considerations such as power and stability requirements limit the realizable coupling. For stability in the infinite lattice, $\xi < 1$ is required to ensure that the eigenvalues Ω for Eq. 3 are real and the response is bounded.

In this study, $\xi = 0.79$ is selected, to observe the impact of an enhanced electromechanical coupling $\vartheta_{NC} = 2$. The same parametric analysis that was conducted in Section 3.2 for the metamaterial with no negative capacitance ($\xi = 0$ and $\vartheta = 0.42$) is conducted for the metamaterial with enhanced coupling ($\xi = 0.79$ and $\vartheta_{NC} = 2$), and the achievable operating region for the topological interface state is shown enclosed by black dashed lines in Fig. 4a. As can be seen by the comparison of Fig. 4a and Fig. 3b, the achievable operating region is greatly enlarged by the addition of negative capacitance circuitry and enhanced electromechanical coupling. The frequency range of the operating region is extended to lower frequencies, now covering $\Omega_{\text{Dirac}} = 3.2$ to $\Omega_{Dirac} = 11$ (see extension represented by the orange box in Fig. 2b). This corresponds to a 15% increase in achievable frequency range, greatly enhancing the adaptivity of the frequency for the topological interface state. In addition, there is a 67% increase in the range of allowable $|\beta|$, as perturbations to the inductance parameter up to $|\beta| = 0.05$ are now included in the achievable operating region. As demonstrated in Sec. 3.2, more localized interface states can be achieved with a larger circuit inductance perturbation $|\beta|$. Figure 4b contains an interface mode shape for $\Omega_{Dirac} = 9$ and $|\beta| = 0.04$ (marked with ★), with a highly localized displacement achieved at the interface. Since $|\beta|$ can be selected to be larger after the addition of negative capacitance, this interface mode shape is noticeably more localized than the interface mode shapes obtained in Fig. 3b, where the maximum allowable $|\beta|$ is 0.015 for $\Omega_{Dirac} = 9$ and $\xi = 0$. This result holds regardless of the specified Ω_{Dirac}, as the $|\beta|$ values defining the rightmost boundary of the achievable operating region for $\xi = 0.79$ (dashed black line in Fig. 4a) are larger than the corresponding $|\beta|$ values for $\xi = 0$ (Fig. 3b), for all Ω_{Dirac}. In addition to granting greater mode localization, larger $|\beta|$ along the rightmost boundary of the achievable operating region also facilitates the achievement of a larger relative bandgap $\Omega_{bandgap-relative}$ for any Ω_{Dirac}. The larger $\Omega_{bandgap-relative}$ associated with $\xi = 0.79$ indicates a larger potential operating bandwidth for an isolated topological interface state regardless of the chosen Ω_{Dirac}. For example, if a design criteria were to require maximization of operating bandwidth under fixed system parameters, $\Omega_{bandgap-relative-max} = 0.019$ for $\xi = 0.79$ ($|\beta| = 0.04$ and $\Omega_{Dirac} = 9$, ★ in Fig. 4a), which is more than three times larger than $\Omega_{bandgap-relative-max} = 0.006$ for $\xi = 0$ ($|\beta| = 0.015$ and $\Omega_{Dirac} = 9$, ★ in Fig. 3b).

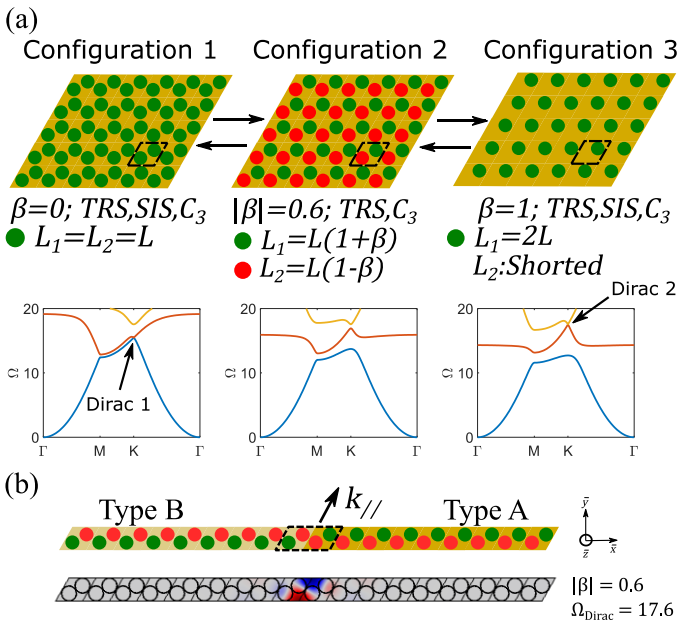

FIGURE 5: (a) Schematics for lattice Configuration 1 (β = 0), Configuration 2 ($\beta \neq 0$), and Configuration 3 (β = 1). Unit cell is enclosed in dashed black lines; green and red circles indicate electrode geometry connected to circuits. Electrodes that are connected to shorted circuits in Configuration 3 are omitted for clarity. Below the schematics are band diagrams calculated from the PWE method for Ω_t = 23 and ϑ= 0.42, with Dirac points highlighted for Configuration 1 and Configuration 3. (b) Finite strip that contains an interface (enclosed by dashed black box) between Type A and Type B unit cells of Configuration 2. Interface mode shape that is generated from dispersion analysis of finite strip defined with the unit cells parameters Ω_{Dirac} = 17.6 and $|\beta|$ = 0.6.

5 LATTICE RECONFIGURATION

Apart from the enhancement of electromechanical coupling using negative capacitance, the adaptivity of the proposed piezoelectric metamaterial also enables lattice reconfiguration. In this section, the capability of the metamaterial to achieve a second Dirac point through lattice reconfiguration and its implications on adaptive topological wave propagation are investigated.

Schematics for three achievable lattice configurations and corresponding band structures calculated from the PWE method (Eq. 3) are shown in Fig. 5a. For this analysis, Ω_t = 23 and ϑ= 0.42 (no negative capacitance is connected to independently show the effect of lattice reconfiguration). Configuration 1 is the honeycomb lattice structure with all circuits defined to be identical ($\beta = 0, L_1 = L_2 = L$ in unit cell). As shown in Sec. 3.1 using the PWE method, the band structure for this configuration contains a Dirac point formed from the first and second bands that is protected by TRS, SIS, and C_3 lattice symmetry (see Dirac 1 in band structure, Fig. 5a). TRS, SIS, and C_3 lattice symmetry are also achievable with a triangular lattice structure, which can be realized in the proposed piezoelectric metamaterial by shorting one of the two circuits in the unit cell (e.g., β = 1, L_1 = $2L$, circuit 2 is shorted, see Configuration 3 in Fig. 5a). Analysis of the band structure for Configuration 3 reveals that a Dirac point formed from the second and third bands is identified at Ω_{Dirac} = 17.6 (Dirac 2 in Fig. 5a). Previous studies on photonic metamaterials with triangular lattice structures also observe this Dirac point forming from the second and third bands, validating the result [33–35]. Thus, by switching between Configuration 1 (β = 0) and Configuration 3 (β = 1), the proposed metamaterial can achieve two separate Dirac points, Dirac 1 and Dirac 2. In contrast to Dirac 1, Dirac 2 is not frequency tunable (i.e., Ω_{Dirac} = 17.6 $\forall$ Ω_t for Dirac 2). However, as shown in Sec 3.2, the achievable operating region for topological interface states derived from Dirac 1 is constrained between Ω_{Dirac} = 4.2 and Ω_{Dirac} = 11. Thus, the frequency of Dirac 2 (Ω_{Dirac} = 17.6) provides an avenue to enhance the achievable operating region through the realization of higher frequency topological interface states.

Section 3.1 outlines how a bandgap is formed from Dirac 1 by breaking SIS (specifying $\beta \neq 0$), and topologically distinct lattices are defined and joined at an interface to achieve a topological interface state. A similar method is applied to Dirac 2. To open a bandgap from Dirac 2, SIS is broken by specifying $\beta \neq 1$, represented in Fig. 5a by Configuration 2. For Configuration 2, a full bandgap $\Omega_{bandgap}$ = 0.6 is formed between the second and third bands by specifying $|\beta|$ = 0.6 (Fig. 5a, Configuration 2). The valley Chern numbers are calculated to evaluate the topological characteristics of these bands. For β = 0.6, C^A_{v-2}= 0.3 and C^A_{v-3} = -0.3, indicating a nontrivial topological charge in terms of the QVHE (see discussion in Sec 3.1). In contrast, C^B_{v-2}= -0.3 and C^B_{v-3} = 0.3 for β = -0.6, indicating Type A and Type B lattices with $|\beta|$ = 0.6 are topologically distinct. Thus, if Type A and Type B lattices with $|\beta|$ = 0.6 are joined at an interface, a topological transition occurs, facilitating the emergence of a topological interface state within the bandgap. In addition, since $|C_v| \geq 0.3$, the prescribed circuit parameters ($|\beta|$ = 0.6, Ω_t = 23, Ω_{Dirac} = 17.6) would be included in the achievable operating region for topological interface states defined in Sec. 3. The associated $\Omega_{bandgap-relative}$ is equal to 0.035, which is far greater than the maximum relative bandgap found within the achievable operating region reported in Sec. 3.2, $\Omega_{bandgap-relative-max}$ = 0.006. With Dirac 2 located at Ω_{Dirac} = 17.6 and $\Omega_{bandgap}$ = 0.6, topological interface states derived from Dirac 2 that are contained within the achievable operating region are realizable from Ω = 17 to Ω = 17.6 (note: the top edge of the bandgap is fixed at 17.6). Thus, topological interface states derived from Dirac 2 are achievable at higher frequencies than are achievable from Dirac 1, and the total range of frequencies contained by the achievable operating region is enhanced by 8% (when compared to the baseline achievable operating region Ω = 4.2 and Ω = 11, blue box in Fig. 2b). The enhancement of the frequency tunability of the proposed metamaterial gained from this lattice reconfiguration is represented by the green boxed region in Fig. 2b.

To confirm the emergence of a topological interface state from Dirac 2 near Ω_{Dirac}= 17.6, COMSOL is used to generate the band structure for a finite strip with Type A and Type B lattices joined at an interface. As in Sec. 3.2, the edges are fixed

and a periodic boundary condition is applied in the $k_{//}$ direction (Fig. 5b). Figure 5b contains an interface mode shape with a localized displacement that is obtained from the band structure for the finite strip with $|\beta| = 0.6$, $\Omega_t = 23$, and $\Omega_{Dirac} = 17.6$.

6 CONCLUSIONS

In this study, negative capacitance circuitry and lattice reconfiguration are investigated as a means to enhance the adaptive capabilities and performance of a piezoelectric topological metamaterial. The plane wave expansion method is used to identify distinct Dirac cones within the unit cell and show that topological interface states can be achieved via circuit parameter perturbations. Performance metrics ($\boldsymbol{\Omega_{relative\ bandgap}}$ and $|\boldsymbol{C_v}|$) are calculated to quantify the potential operating bandwidth and topological protection for the interface states under specified circuit parameters. To evaluate the adaptivity of the metamaterial, a parametric analysis is undertaken to identify an achievable operating region where interface states with sufficient operating bandwidth and topological protection can be realized. Exploration of the achievable operating region shows that the frequency of the topological interface state and the displacement localization of the associated interface modes can be tailored over a wide range using circuit parameters.

Results indicate that the addition of negative capacitance circuity enhances the range of frequencies and interface mode shapes contained in the achievable operating region, greatly expanding the adaptive metamaterial capabilities. This expansion of the achievable operating region facilitates the achievement of topological interface states with a greater level of displacement localization and augments the maximum potential operating bandwidth. An additional method to enhance the performance and adaptivity of the metamaterial is lattice reconfiguration. The ability to achieve two separate Dirac points in an adaptive elastic metamaterial exhibiting the QVHE is demonstrated and explored for the first time. By reconfiguring the lattice to a triangular lattice structure, the frequency range of the achievable operating region is further enhanced, and higher frequency interface states can be achieved (when compared to the baseline achievable operating region). Thus, both the connection of negative capacitance circuitry and lattice reconfiguration greatly enhance the adaptivity and performance of the topological piezoelectric metamaterial. The ability to tune topological interface states over a wider frequency range and achieve more localized mode shapes would allow the metamaterial to be much more adaptive to changing external conditions and enhance performance for a variety of operating requirements. These attributes would be advantageous in applications where adaptive wave control can improve performance, such as vibration isolation, energy harvesting, and wave filtering.

ACKNOWLEDGMENTS

This research is funded by the National Science Foundation under Award No. 1661568. P.D. also acknowledges financial support from the Rackham Merit Fellowship at the University of Michigan.

REFERENCES

[1] Huber, Sebastian D. “Topological Mechanics.” *Nature Physics* Vol. 12 No. 7 (2016): pp. 621–623.

[2] Ma, Guancong, Xiao, Meng, and Chan, C.T. “Topological Phases in Acoustic and Mechanical Systems.” *Nature Reviews Physics* Vol. 1 No. 4 (2019): pp. 281–294. DOI https://doi.org/10.1038/s42254-019-0030-x.

[3] Hussein, Mahmoud I., Leamy, Michael J., and Ruzzene, Massimo. “Dynamics of Phononic Materials and Structures: Historical Origins, Recent Progress, and Future Outlook.” *Applied Mechanics Reviews* Vol. 66 No. 4 (2014): p.040802. DOI https://doi.org/10.1115/1.4026911.

[4] Zhu, Hongfei, Liu, Ting-Wei, and Semperlotti, Fabio. “Design and Experimental Observation of Valley-Hall Edge States in Diatomic-Graphene-like Elastic Waveguides.” *Physical Review B* Vol. 97 No. 17 (2018): p.174301. DOI https://doi.org/10.1103/PhysRevB.97.174301.

[5] Vila, Javier, Pal, Raj Kumar, and Ruzzene, Massimo. “Observation of Topological Valley Modes in an Elastic Hexagonal Lattice.” *Physical Review B* Vol. 96 No. 13 (2017): p.134307. DOI https://doi.org/10.1103/PhysRevB.96.134307.

[6] Pal, Raj Kumar, and Ruzzene, Massimo. “Edge Waves in Plates with Resonators: An Elastic Analogue of the Quantum Valley Hall Effect.” *New Journal of Physics* Vol. 19 No. 2 (2017): p.025001. DOI https://doi.org/10.1088/1367-2630/aa56a2.

[7] Swinteck, N., Matsuo, S., Runge, K., Vasseur, J.O., Lucas, P., and Deymier, P.A. “Bulk Elastic Waves with Unidirectional Backscattering-Immune Topological States in a Time-Dependent Superlattice.” *Journal of Applied Physics* Vol. 118 No. 6 (2015): p.063103. DOI https://doi.org/10.1063/1.4928619.

[8] Nash, Lisa M., Kleckner, Dustin, Read, Alismari, Vitelli, Vincenzo, Turner, Ari M., and Irvine, William T.M. “Topological Mechanics of Gyroscopic Metamaterials.” *Proceedings of the National Academy of Sciences* Vol. 112 No. 47 (2015): pp.14495–14500. DOI https://doi.org/10.1073/pnas.1507413112.

[9] Süsstrunk, Roman and Huber, Sebastian D. “Observation of Phononic Helical Edge States in a Mechanical Topological Insulator.” *Science* Vol. 349 No. 6243 (2015): pp. 47–50. DOI https://doi.org/10.1126/science.aab0239.

[10] Mousavi, S. Hossein, Khanikaev, Alexander B., and Wang, Zheng. “Topologically Protected Elastic Waves in Phononic Metamaterials.” *Nature Communications* Vol. 6 (2015): p.8682. DOI https://doi.org/10.1038/ncomms9682.

[11] Liu, Ting-Wei, and Semperlotti, Fabio. “Tunable Acoustic Valley–Hall Edge States in Reconfigurable Phononic Elastic Waveguides.” *Physical Review Applied* Vol. 9 No. 1 (2018): p. 014001. DOI https://doi.org/10.1103/PhysRevApplied.9.014001.

[12] Tang, Kun, Makwana, Mehul P., Craster, Richard V., and Sebbah, Patrick. “Observations of Symmetry Induced Topological Mode Steering in a Reconfigurable Elastic Plate.” *ArXiv Preprint* ArXiv:1910.08172 (2019). http://arxiv.org/abs/1910.08172.

[13] Li, Shuaifeng, Zhao, Degang, Niu, Hao, Zhu, Xuefeng, and Zang, Jianfeng. "Observation of Elastic Topological States in Soft Materials." *Nature Communications* Vol. 9 (2018): p. 1370. DOI https://doi.org/10.1038/s41467-018-03830-8.

[14] Liu, Heng, Huo, Shao-Yong, Feng, Lu-Yang, Huang, Hong-Bo, and Chen, Jiu-Jiu. "Thermally Tunable Topological Edge States for In-Plane Bulk Waves in Solid Phononic Crystals." *Ultrasonics* Vol. 94 (2019): pp. 227–234. DOI https://doi.org/10.1016/j.ultras.2018.09.006.

[15] Zhang, Quan, Chen, Yi, Zhang, Kai, and Hu, Gengkai. "Programmable Elastic Valley Hall Insulator with Tunable Interface Propagation Routes." *Extreme Mechanics Letters* Vol. 28 (2019): pp. 76–80. DOI https://doi.org/10.1016/j.eml.2019.03.002.

[16] Riva, E., Quadrelli, D. E., Cazzulani, G., and Braghin, F. "Tunable In-Plane Topologically Protected Edge Waves in Continuum Kagome Lattices." *Journal of Applied Physics* Vol. 124 No. 16 (2018): p. 164903. DOI https://doi.org/10.1063/1.5045837.

[17] Darabi, Amir, Collet, Manuel and Leamy, Michael J. "Experimental Realization of a Reconfigurable Electroacoustic Topological Insulator." *ArXiv Preprint* ArXiv:1911.09608 (2019). http://arxiv.org/abs/1911.09608.

[18] Zhou, Weijian, Wu, Bin, Chen, Zhenyu, Chen, Weiqiu, Lim, C. W., and Reddy, J. N. "Actively Controllable Topological Phase Transition in Homogeneous Piezoelectric Rod System." *Journal of the Mechanics and Physics of Solids* Vol. 137 (2020): p. 103824. DOI https://doi.org/10.1016/j.jmps.2019.103824.

[19] Dorin, Patrick and Wang, K. W. "Reconfigurable Elastic Quantum Valley Hall Edge States in a Piezoelectric Topological Metamaterial." *Proceedings of SPIE 11381, Health Monitoring of Structural and Biological Systems IX*. 11381-47. April 27-May 1, 2020.

[20] Tang, Jiong, and Wang, K.W. "Active-Passive Hybrid Piezoelectric Networks for Vibration Control: Comparisons and Improvement." *Smart Materials and Structures* Vol. 10 No. 4 (2001): pp. 794–806.

[21] Tang, Jiong, and Wang, K.W. *Adaptive Structural Systems with Piezoelectric Transducer Circuitry*. Springer, New York (2008).

[22] Meirovitch, Leonard. *Analytical Methods in Vibrations*. MacMillan, New York (1967).

[23] Tiersten, Harry F. *Linear Piezoelectric Plate Vibrations: Elements of the Linear Theory of Piezoelectricity and the Vibrations of Piezoelectric Plates*. Springer, New York (2013).

[24] Graff, Karl. *Wave Motion in Elastic Solids*. Dover Publications, New York (1991).

[25] Xiao, Yong, Wen, Jihong, and Wen, Xisen. "Flexural Wave Band Gaps in Locally Resonant Thin Plates with Periodically Attached Spring-Mass Resonators." *Journal of Physics D: Applied Physics* Vol. 45 No. 19 (2012): p. 195401. DOI https://doi.org/10.1088/0022-3727/45/19/195401.

[26] Torrent, Daniel, Mayou, Didier, and Sánchez-Dehesa, José. "Elastic Analog of Graphene: Dirac Cones and Edge States for Flexural Waves in Thin Plates." *Physical Review B* Vol. 87 No. 11 (2013): p. 115143. DOI https://doi.org/10.1103/PhysRevB.87.115143.

[27] Berry, Michael Victor. "Quantal Phase Factors Accompanying Adiabatic Changes." *Proceedings of the Royal Society of London. A. Mathematical and Physical Sciences* Vol. 392 No. 1802 (1984): pp. 45–57. DOI https://doi.org/10.1142/9789813221215_0006.

[28] Yao, Wang, Yang, Shengyuan A., and Niu, Qian. "Edge States in Graphene: From Gapped Flat-Band to Gapless Chiral Modes." *Physical Review Letters* Vol. 102 No. 9 (2009): p. 096801. DOI https://doi.org/10.1103/PhysRevLett.102.096801.

[29] Xiao, Di, Yao, Wang, and Niu, Qian. "Valley-Contrasting Physics in Graphene: Magnetic Moment and Topological Transport." *Physical Review Letters* Vol. 99 No. 23 (2007): p. 236809. DOI https://doi.org/10.1103/PhysRevLett.99.236809.

[30] Du, Zongliang, Chen, Hui, and Huang, Guoliang. "Optimal Quantum Valley Hall Insulators by Rationally Engineering Berry Curvature and Band Structure." *Journal of the Mechanics and Physics of Solids* Vol. 135 (2020): p. 103784. DOI https://doi.org/10.1016/j.jmps.2019.103784.

[31] Qian, Kai, Apigo, David J., Prodan, Camelia, Barlas, Yafis, and Prodan, Emil. "Topology of the Valley-Chern Effect." *Physical Review B* Vol. 98 No. 15 (2018): p. 155138. DOI https://doi.org/10.1103/PhysRevB.98.155138.

[32] Nguyen, B. H., Zhuang, X., Park, H. S., and Rabczuk. T. "Tunable Topological Bandgaps and Frequencies in a Pre-Stressed Soft Phononic Crystal." *Journal of Applied Physics* Vol. 125 No. 9 (2019): p. 095106. DOI https://doi.org/10.1063/1.5066088.

[33] Kim, N. Y., Kusudo, K., Löffler, A., Höfling, S., Forchel, A. and Yamamoto, Y. "Exciton-Polariton Condensates near the Dirac Point in a Triangular Lattice." *New Journal of Physics* Vol. 15 (2013): p. 035032. DOI https://doi.org/10.1088/1367-2630/15/3/035032.

[34] Zhang, Xiangdong. "Observing Zitterbewegung for Photons near the Dirac Point of a Two-Dimensional Photonic Crystal." *Physical Review Letters* Vol. 100 No. 11 (2008): p. 113903. DOI https://doi.org/10.1103/PhysRevLett.100.113903.

[35] Plihal, M., and Maradudin, A. A. "Photonic Band Structure of Two-Dimensional Systems: The Triangular Lattice." *Physical Review B* Vol. 44 No. 16 (1991): pp. 8565–8571. https://doi.org/10.1103/PhysRevB.44.8565.